



**AIAA 2004-0759**

**Agglomeration Multigrid for an  
Unstructured-Grid Flow Solver**

Mohagna J. Pandya  
Swales Aerospace, Hampton, Virginia

Neal T. Frink  
NASA Langley Research Center, Hampton, Virginia

**42nd AIAA Aerospace Sciences  
Meeting & Exhibit**  
5-8 January 2004 / Reno, NV

## AGGLOMERATION MULTIGRID FOR AN UNSTRUCTURED GRID FLOW SOLVER

**Mohagna J. Pandya**<sup>§</sup>

Swales Aerospace, Hampton, VA 23681

**Neal T. Frink**<sup>\*</sup>

Configuration Aerodynamics Branch, AAAC  
NASA Langley Research Center, Hampton, VA 23681

### Abstract

An agglomeration multigrid scheme has been implemented into the sequential version of the NASA code USM3Dns, tetrahedral cell-centered finite volume Euler/Navier-Stokes flow solver. Efficiency and robustness of the multigrid-enhanced flow solver have been assessed for three configurations assuming an inviscid flow and one configuration assuming a viscous fully turbulent flow. The inviscid studies include a transonic flow over the ONERA M6 wing and a generic business jet with flow-through nacelles and a low subsonic flow over a high-lift trapezoidal wing. The viscous case includes a fully turbulent flow over the RAE 2822 rectangular wing. The multigrid solutions converged with 12%-33% of the Central Processing Unit (CPU) time required by the solutions obtained without multigrid. For all of the inviscid cases, multigrid in conjunction with an explicit time-stepping scheme performed the best with regard to the run time memory and CPU time requirements. However, for the viscous case multigrid had to be used with an implicit backward Euler time-stepping scheme that increased the run time memory requirement by 22% as compared to the run made without multigrid.

### Introduction

Unstructured-grid (USG) methodology has emerged as a mature computational fluid dynamics (CFD) tool for rapid aerodynamics analysis and design of complex configurations. It offers a substantially reduced turnaround time for CFD solutions due primarily to the ease and speed at which unstructured grids can be generated. Key components of the USG methodology have been consolidated into a flow analysis tool called the NASA Tetrahedral Unstructured Software System (TetrUSS). The

TetrUSS system [1] is a loosely integrated, user-friendly software that comprises of a geometry setup tool GridTool [2], a tetrahedral grid generator VGRIDns [3, 4], and a flow solver USM3Dns [5, 6].

Traditional flow solvers based on a single grid tend to suffer from a degradation of the asymptotic convergence rate as the mesh is refined. The relaxation schemes in these flow solvers efficiently eliminate high frequency error modes but fail to reduce low frequency errors that hamper the flow convergence [7]. This difficulty can be circumvented by multigrid methodology [8]. In this method a sequence of meshes is employed such that a smooth error on a fine mesh appears as a high frequency error on a coarser mesh, where it can be efficiently reduced by a relaxation scheme. Multigrid methods have been successfully utilized by several structured grid Euler/Navier-Stokes solvers where a sequence of optimized coarser meshes can be readily generated from a base fine grid. In the past decade, various multigrid strategies [9-13] have also been successfully demonstrated for the unstructured grid flow solvers. These strategies include overset grids [9], where multiple coarser grids are separately constructed, and agglomerated grids [10-13], where coarser grids are constructed by coalescing neighboring fine grid cells. A primary benefit of an agglomeration multigrid method is that it spares a user the effort of manually generating multiple coarser grids, which may not even be feasible for complex geometries. Most of the multigrid implementations involving unstructured grids are based on node-centered schemes with a few exceptions [11]. Current work seeks to evaluate benefits of multigrid technique in a cell-centered flow code and to add to a relatively sparse body of literature in this arena.

### Methodology

An agglomeration multigrid technique is implemented in an unstructured grid based flow code USM3Dns. USM3Dns is a tetrahedral cell-centered, finite volume Euler and Navier-Stokes flow solver. Each tetrahedron forms the elemental control volume

---

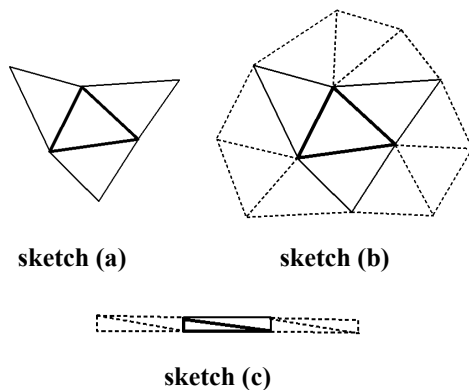
<sup>§</sup> Research Engineer

<sup>\*</sup> Senior Research Engineer, Associate Fellow, AIAA

Copyright © 2003 by the American Institute of Aeronautics and Astronautics, Inc. No copyright is asserted in the United States under Title 17, U.S. Code. The U.S. Government has a royalty-free license to exercise all rights under the copyright claimed herein for governmental purposes. All other rights are reserved by the copyright owner.

for the spatial discretization. Inviscid flux quantities are computed across each cell face using Roe's flux-difference splitting [14]. Spatial discretization is accomplished by a novel reconstruction process [15] which is based on an analytical formulation for computing solution gradients within tetrahedral cells. The solution is advanced to a steady state by an implicit backward Euler time-stepping scheme [16]. Flow turbulence effects are modeled by either the one equation model of Spalart-Allmaras (S-A) [17], or one of the recently implemented [18] two equation models of  $k-\epsilon$  and Menter's Shear Stress Transport (SST). The S-A model can be optionally coupled with a wall function boundary condition to reduce the number of cells in the sublayer region of the boundary layer.

The coarse grids are constructed in two steps by volume agglomeration. In the first step, all the fine grid cells attached to the body surface or a far-field boundary are identified and merged with its neighboring (only those cells are eligible that are not already assigned to a previous coarser cell) cells to form a new coarser cell. After all of these prioritized boundary cells are assigned to a coarser cell, an unassigned fine grid cell on the agglomeration front is picked in a random order and merged with its eligible neighbors to form a new coarser cell. The schematic view of this procedure is outlined in sketch (a) below where a seed cell (the first cell assigned to a newly defined coarse cell) is shown with thick lines and its unassigned neighbors are shown with thinner lines. The procedure is repeated until all the fine grid cells are assigned to a coarser parent cell. In the second step, a set of fine grid faces at the interface of a given pair of coarser cells is used to render a single resultant face [19]. This step reduces the number of faces in a coarse grid that has a direct bearing on the computational efficiency of the agglomeration multigrid technique.



Two variants of the agglomeration strategy illustrated previously in the step 1 are also available. In the first

alternative which may be best suited for an isotropic grid associated with inviscid solutions, neighboring cells surrounding all the vertices of the seed cell are agglomerated as shown in sketch (b). In sketch (b), the additional neighbors (compared to the neighbors shown in sketch (a)), are shown with the dashed lines. The second alternative for the agglomeration procedure is illustrated in sketch (c), which may be the most suitable method for highly stretched cells inherent in a boundary layer grid corresponding to the viscous solutions. In this procedure, a coarse cell is formed by a sequential directional-coarsening, where a cell coarsening in the body-normal direction (that generates prisms for the tetrahedral grid) is followed by a coarsening in the lateral (stream- and span-wise) directions (that agglomerates the neighboring prisms). A preliminary evaluation of all the three strategies has revealed that the strategy illustrated in sketch (a) is more robust and therefore it has been chosen for all the results presented in the later section.

The coarse grid generation process is embedded within the flow solver itself. The generation of multiple coarser grids requires a trivial amount of CPU time.

The equations on coarse grids are discretized using the techniques similar to that used for the finest tetrahedral grid. One notable difference is that coarse grid inviscid flux calculation procedure is first order accurate. Also, the turbulence model equations are not solved on the coarser grids. The turbulence effects on the coarse grids are derived from the finest grid values. The multigrid solution is advanced in time by either a three stage Runge-Kutta scheme or an implicit backward Euler time marching scheme. Local time stepping is employed for all grids. The flow solution is transferred from a fine grid to a coarser grid by a volume-weighted averaging whereas the prolongation of correction from a coarse grid to a finer grid is based on a simple injection. The restriction of the residuals to a coarser grid is accomplished by summation of the residuals of fine grid cells that define a coarser cell. One relaxation sweep is performed at every grid level to smooth the high frequency error components. The relaxation step is followed by a coarse grid correction to efficiently reduce the low frequency errors. The corrections generated by a coarse grid are smoothed before transferring them to a finer grid. Typically, one (V-cycle) or two (W-cycle) multigrid cycles are performed for the coarse grid correction.

## Results

The tetrahedral unstructured grids around the following test configurations have been generated using the grid generator VGRIDns. For the multigrid runs, the tetrahedral grid serves as the finest grid from which all coarser grids are generated using the volume agglomeration technique described earlier. Therefore, the tetrahedral grid will be referred to as the baseline grid in the discussion below. For all the test cases, flow fields have been computed using the solver USM3Dns. The non-multigrid solutions corresponding to a single baseline grid will be referred to as the baseline solutions hereafter.

### Inviscid Cases

The inviscid multigrid implementation has been tested on three different configurations, namely, the ONERA M6 wing, a generic business jet with flow-through nacelles, and a high-lift trapezoidal wing. For all the test cases, flow fields have been computed based on both, an explicit and an implicit time marching schemes with and without multigrid. However, for all the cases the multigrid solution that used an explicit scheme outperformed the one that used an implicit scheme, with respect to CPU time as well as runtime memory. Therefore, the multigrid solution based on an implicit scheme will not be shown elaborately.

#### ONERA M6 Wing

The baseline grid for this case consists of 346,939 tetrahedral cells and 702,589 triangular faces. The computational boundary is discretized with 17,422 triangular faces. Based on this underlying grid, four coarser grids have been generated consisting of 123,933, 35,746, 7,470 and 1,265 polyhedral cells, respectively, yielding a cell-based average coarsening ratio of 4.1. The coarser grids consist of 406,356, 189,291, 52,158 and 9,955 polygonal faces, respectively. A view of the baseline and four coarser grids on the wing surface has been presented in the Figure 1. A histogram has been presented in the Figure 2 that shows the number of coarse grid cells that comprises of a certain number of constituent finer grid cells of the preceding level.

The flow field around the present configuration has been computed considering a free stream Mach number of 0.84 and an angle-of-attack of  $3.06^\circ$ . Multigrid solutions have been generated based on five (baseline and four coarse) grids described previously, using both, V- and W-cycle. Convergence history of the flow residue, the lift coefficient and the

drag coefficient corresponding to the V- and W-cycle multigrid explicit solutions and the baseline explicit solution has been displayed in the Figure 3. Although not shown in the figure, V- and W-cycle multigrid implicit and baseline implicit solutions have also been obtained for this case. The convergence characteristics of various solution techniques have been summarized in the Table 1 that describes the CPU time required to drive the lift coefficient to three different levels of tolerance. The run time memory and the CPU time per iteration needed for various methods of solution are listed in the Table 2.

The W-cycle multigrid explicit run has been found to be the most competitive of all the multigrid runs. The W-cycle multigrid explicit scheme yielded the converged solution more than ten times faster as compared to the baseline explicit scheme and about four to six times faster as compared to the baseline implicit solution. Figure 4 presents a comparison of the surface pressure coefficients obtained using the W-cycle multigrid explicit and the baseline implicit methods at two span wise cross-sections of the wing. The multigrid solution is nearly identical to the baseline implicit solution, as expected. For the subsequent cases, multigrid convergence characteristics will be demonstrated for the W-cycle only.

#### Generic Business Jet

The baseline grid for this case consists of 784,078 tetrahedral cells and 1,585,006 triangular faces. The computational boundary is discretized with 33,700 triangular faces. Based on this grid, four coarser grids have been generated consisting of 280,627, 79,868, 16,692 and 2,870 polyhedral cells, respectively, yielding a cell-based average coarsening ratio of 4.1. The coarser grids consist of 919,074, 424,086, 117,317 and 22,617 polygonal faces, respectively.

A view of the baseline body surface grid is presented in the Figure 5. The flow field around this configuration has been computed for a free stream Mach number of 0.75 and an angle-of-attack of  $3^\circ$ . The W-cycle multigrid explicit solution has been obtained using the base grid and four coarser grids described previously. The surface Mach number contours for this solution have been shown in the Figure 5. Convergence of the flow residue, the lift coefficient and the drag coefficient corresponding to the W-cycle multigrid explicit, the baseline explicit and the baseline implicit methods has been demonstrated in the Figure 6. The multigrid solution rendered the converged lift and drag coefficients more than fifteen times faster compared to the

baseline explicit solution and more than four times faster compared to the baseline implicit solution.

Subsequently, an assessment of the effect of grid density on the multigrid convergence characteristics has been made. For this purpose, in addition to the grid used thus far, two more grids, namely, a coarser and a finer grid, have been generated. The grid used thus far has been designated as medium grid. The coarse grid has 150,362 tetrahedral cells whereas the fine grid has 1,204,476 tetrahedral cells. The computational boundary has been represented with 11,706 triangular faces in the coarse grid and 48,430 triangular faces in the fine grid. Both of these grids have been used to obtain the W-cycle multigrid explicit and implicit solutions. For this purpose, four agglomerated coarse grids have been generated from each of these two baseline grids. The baseline explicit and implicit solutions have also been generated for the two baseline grids. Convergence of the flow residue, the lift coefficient and the drag coefficient corresponding to the W-cycle multigrid explicit and the baseline explicit inviscid solutions obtained on three different grid densities has been shown in the Figure 7. A summary of the number of iterations and the CPU time required by various methods to obtain the lift coefficient within 0.1 % of its final value for coarse and fine base grid has been presented in the Table 3. Convergence of the multigrid solutions has been found to be much less dependent on the grid density as compared to that of the baseline solutions.

### Trapezoidal Wing

This geometry represents a generic high-lift configuration with a leading-edge slat and a trailing-edge flap. The baseline grid for this case consists of 862,670 tetrahedral cells and 1,757,461 triangular faces. The computational boundary is discretized with 64,242 triangular faces. Four coarser grids have been generated consisting of 307,879, 86,953, 17,888 and 3,059 polyhedral cells, respectively, yielding a cell-based average coarsening ratio of 4.1. The coarser grids consist of 1,015,282, 459,568, 124,778 and 24,044 polygonal faces, respectively. The baseline grid on the body surface has been presented in the Figure 8.

The flow field around this configuration has been computed for a free stream Mach number of 0.2 and an angle-of-attack of  $8^\circ$ . The W-cycle multigrid explicit solution has been obtained using the baseline grid and four coarser grids described previously. The surface Mach number contours for this solution have been shown in the Figure 8. The solutions have also

been computed using the baseline explicit and the baseline implicit methods. The baseline explicit solution failed to converge despite a lower Courant-Freidrich-Lewis (CFL) number and has been stopped after 3500 cycles. Convergence of the flow residue, the lift coefficient and the drag coefficient corresponding to the W-cycle multigrid explicit, the baseline explicit and the baseline implicit methods has been demonstrated in the Figure 9. The multigrid explicit solution converges about three times faster than the baseline implicit solution. However, for this case the convergence of the multigrid explicit technique has somewhat degraded.

### **Viscous Case**

Efficacy of the present multigrid implementation for a viscous turbulent flow analysis has been assessed on one case, namely, RAE 2822 rectangular wing with a span of 20% of the chord. The baseline grid for this case consists of 86,314 tetrahedral cells and 190,110 triangular faces. The computational boundary is discretized with 34,964 triangular faces. The grid consists of 23 points across the boundary layer at any location on the wing. The grid spacing in the normal direction at the wing surface is  $4.2 \times 10^{-6}$ . Three coarser grids have been generated consisting of 29,899, 9,462 and 2,369 polyhedral cells, respectively, yielding a cell-based average coarsening ratio of 3.3. A lower grid coarsening ratio for this case, as compared to the previous inviscid cases, is due to the fact that the grid coarsening in the span wise direction is constrained due to the close proximity of the end wall boundaries. Additionally, for the current case only three coarse grid levels have been used whereas all the previous cases have used four levels of coarse grid. It may be noted that for all the previous cases, the fourth coarse grid level has substantially contributed to the enhancement of the overall grid coarsening ratio. The coarser grids consist of 23,638, 13,663 and 5,375 polygonal faces, respectively. A close up view of the grid around the airfoil surface for the baseline, the first and the third level coarse grid has been presented in the Figure 10.

The flow field around the RAE 2822 wing has been computed for a free stream Mach number of 0.75, an angle-of-attack of  $2.72^\circ$  and a Reynolds number of  $6.2 \times 10^6$ . For the presently used baseline grid and Reynolds number, an average  $Y^+$  is 1 for the first layer of nodes above the wing surface. Turbulence effects on the tetrahedral grid have been modeled using the one-equation S-A model.

The multigrid solution based on the W-cycle failed to satisfactorily converge for this case. Therefore, V-

cycle has been used for the multigrid runs. Convergence of various solutions based on the V-cycle multigrid explicit, the V-cycle multigrid implicit, the baseline explicit and the baseline implicit methods has been summarized in the Table 4. The runtime memory and the CPU time needed for each of the above solution methods has been documented in the Table 5. It is evident from the Table 4 that the solution based on an explicit scheme, either with or without multigrid, fails to offer a viable alternative to the solution based on an implicit scheme. Therefore, a comparison of the flow residue, the lift coefficient and the drag coefficient convergence, shown in the Figure 11, has been restricted to the V-cycle multigrid implicit and the baseline implicit methods. It is apparent from the Table 4 and the Figure 11 that the multigrid solution as compared to the baseline solution converges faster by at least a factor of three. The surface pressure coefficients obtained using the V-cycle multigrid implicit and the baseline implicit methods as well as the measurements [20] have been compared in the Figure 12. It is evident from the figure that the multigrid solution is nearly identical to the baseline implicit solution and matches well with the measurements.

### Concluding Remarks

Agglomeration-based multigrid scheme has been successfully implemented in the sequential version of the tetrahedral cell-centered flow solver USM3Dns. Assessment of the multigrid-enhanced code has been made using three inviscid flow cases and one viscous turbulent flow case. The inviscid results indicate that the W-cycle multigrid in conjunction with an explicit scheme significantly outperforms the baseline implicit method. The W-cycle multigrid explicit method has yielded a converged solution with less than 50% of the memory and 15%-33% of the CPU time required by the baseline implicit scheme. The baseline explicit scheme has performed poorly and cannot be considered as a viable solution method for complex configurations. For the solitary viscous case studied presently, V-cycle multigrid in conjunction with an implicit scheme has delivered a converged solution with 12%-25% of the CPU time required by the baseline implicit scheme. The multigrid implicit scheme has required about 22% more memory as compared to the baseline implicit scheme. For the viscous case, multigrid explicit scheme has performed poorly from the standpoint of the CPU time. The W-cycle multigrid has also failed to exhibit a required degree of the robustness.

Evaluation of the multigrid efficiency for more viscous cases will be continued hereafter. The present

agglomeration strategy yields an average grid-coarsening ratio of 4 which is half the ideal coarsening ratio for a three-dimensional grid. The present multigrid implementation can be further optimized if a more effective grid coarsening strategy can be devised. A comprehensive evaluation of the various agglomeration strategies discussed previously will be necessary for this purpose. Future work will focus on formulating superior grid-coarsening strategy and better relaxation scheme for error smoothing, such as a line implicit method. Finally, multigrid will be implemented in to the parallel version of the flow solver.

### Acknowledgments

Work of the first author was funded by Configuration Aerodynamics Branch, NASA Langley Research Center under contract NAS1-00135. The technical monitor was Dr. Neal Frink. The authors wish to express sincere appreciation to Dr. Dimitri Mavriplis of National Institute of Aerospace, Hampton, VA for providing insight and many valuable suggestions related to the current work. Authors also wish to thank Drs. Pieter Buning and Veer Vatsa of NASA Langley Research Center and Maharaj Bhat of L-3COM Government Services, Bowie, MD for the helpful discussions related to the current work.

### References

1. Frink, N. T., Pirzadeh, S. Z., Parikh, P., Pandya, M. J., Bhat, M. K., "The NASA tetrahedral unstructured software system (TetrUSS)," *The Aeronautical Journal*, Vol. 104, No. 1040, October 2000, pp. 491-499.
2. Samareh, J., "GridTool: A surface modeling and grid generation tool," Proceedings of the Workshop on Surface Modeling, Grid Generation, and Related Issues in CFD Solutions, NASA CP-3291, 9-11 May, 1995.
3. Pirzadeh, S., "Structured background grids for generation of unstructured grids by advancing front method," *AIAA Journal*, Vol. 31, No. 2, February 1993, pp. 257-265.
4. Pirzadeh, S., "Unstructured viscous grid generation by advancing-layers method," *AIAA Journal*, Vol. 32, No. 8, August 1994, pp. 1735-1737.
5. Frink, N. T., "Upwind scheme for solving the Euler equations on unstructured tetrahedral meshes," *AIAA Journal*, Vol. 30, No. 1, January 1992, pp. 70-77.

6. Frink, N. T., "Tetrahedral unstructured Navier-Stokes method for turbulent flows," *AIAA Journal*, Vol. 36, No. 11, November 1998, pp. 1975-1982.
7. Briggs, W. L., "A Multigrid Tutorial," SIAM, Philadelphia, PA, 1987.
8. Brandt, A., "Multigrid Techniques with applications to fluid dynamics: 1984 guide," VKI Lecture Series, March 1984, pp. 1-176.
9. Mavriplis, D. J., "Three-dimensional multigrid Reynolds-averaged Navier-Stokes solver for unstructured meshes," *AIAA Journal*, Vol. 33, No. 3, March 1995, pp. 445-453.
10. Lallemand, M., Steve, H., Dervieux, A., "Unstructured multigridding by volume agglomeration: current status," *Computers Fluids*, Vol. 21, No. 3, 1992, pp. 397-433.
11. Smith, W. A., "Multigrid solution of transonic flow on unstructured grids," Recent Advances and Applications in Computational Fluid Dynamics (Ed. O. Baysal), ASME FED Vol. 103, 1990, pp. 145-152.
12. Mavriplis, D. J., Venkatakrishnan, V., "A 3D agglomeration multigrid solver for the Reynolds-averaged Navier-Stokes equations on unstructured meshes," *International Journal for Numerical Methods in Fluids*, Vol. 23, 1996, pp. 527-544.
13. Mavriplis, D. J., "Viscous flow analysis using a parallel unstructured multigrid solver," *AIAA Journal*, Vol. 38, No. 11, November 2000, pp. 2067-2076.
14. Roe, P., "Characteristic based schemes for the Euler equations," *Annual Review of Fluid Mechanics*, Vol. 18, 1986, pp. 337-365.
15. Frink, N. T., "Recent progress toward a three-dimensional unstructured Navier-Stokes flow solver," AIAA Paper 94-0061, January 1994.
16. Anderson, W., Bonhaus, D., "An implicit upwind algorithm for computing turbulent flows on unstructured grids," *Computers Fluids*, Vol. 23, No. 1, 1994, pp. 1-21.
17. Spalart, P., Allmaras, S., "A one-equation turbulence model for aerodynamic flows," AIAA Paper 92-0439, January 1992.
18. Abdol-Hamid, K. S., Frink, N. T., Deere, K. A., Pandya, M. J., "Propulsion simulations using advanced turbulence models with the unstructured-grid CFD tool, TetrUSS," AIAA Paper 2004-0714, January 2004.
19. Mavriplis, D. J., "Multigrid Techniques for Unstructured Meshes," 26<sup>th</sup> VKI Lecture Series on Computational Fluid Dynamics, Von Karman Institute for Fluid Dynamics, Rhode Saint Genese, Belgium, March 1995.
20. Cook, P., McDonald, M., and Firmin, M., "Airfoil RAE 2822- Pressure Distributions and Boundary Layer Wake Measurement," AR-138, AGARD Paper A6, 1979.

Solution technique	final $C_L$	Alpha EV6-500 CPU time in seconds (number of cycles) required to get $C_L$ within		
		0.3% of final value	0.1% of final value	Five decimal places
Multigrid, V-cycle, explicit	0.288009	2,322 (124)	2,543 (134)	5,789 (281)
Multigrid, W-cycle explicit	0.288078	979 (38)	1,454 (53)	4,081 (136)
No multigrid, explicit	0.288073	31,608 (2,807)	40,612 (3,541)	85,600 (7,210)
Multigrid, V-cycle implicit	0.288063	1,946 (25)	2,182 (28)	4,391 (56)
Multigrid, W-cycle, implicit	0.288093	2,200 (17)	2,592 (20)	6,374 (49)
No multigrid, implicit	0.288044	5,996 (121)	7,746 (156)	14,098 (283)

Table 1: Convergence characteristics of various solution techniques for computing an inviscid flow around the ONERA M6 wing at  $M_\infty = 0.84$ ,  $\alpha = 3.06^\circ$ .

Solution technique	Memory (words/cell)	Time/iteration (Alpha EV6-500 CPU seconds)
Multigrid, V-cycle, explicit	86	21.2
Multigrid, W-cycle explicit	86	31.2
No multigrid, explicit	54	12
Multigrid, V-cycle implicit	213	78.8
Multigrid, W-cycle, implicit	213	130.4
No multigrid, implicit	179	49.9

Table 2: Memory and CPU time per iteration required by various solution techniques for computing an inviscid flow around the ONERA M6 wing case at  $M_\infty = 0.84$ ,  $\alpha = 3.06^\circ$ .

Solution technique	Baseline grid	final $C_L$	Alpha EV6-667 CPU time in seconds (number of cycles) required to get $C_L$ within 0.1% of final value
Multigrid, W-cycle, explicit	Coarse	0.454605	443 (49)
Multigrid, W-cycle, explicit	Fine	0.480468	6,941 (59)
No multigrid, explicit	Coarse	0.455530	9,301 (2,571)
No multigrid, explicit	Fine	0.481214	350,961 (6,088)
Multigrid, W-cycle, implicit	Coarse	0.454399	854 (18)
Multigrid, W-cycle, implicit	Fine	0.480366	10,172 (20)
No multigrid, implicit	Coarse	0.455410	1,435 (85)
No multigrid, implicit	Fine	0.481168	41,641 (221)

Table 3: Summary of the convergence characteristics of various solution techniques for computing an inviscid flow using coarse and fine grids around a generic business jet at  $M_\infty = 0.75$ ,  $\alpha = 3^\circ$ .

Solution technique	final $C_L$	Alpha EV6-667 CPU time in seconds (number of cycles) required to get $C_L$ within		
		0.3% of final value	0.1% of final value	Five decimal places
Multigrid, V-cycle, explicit	0.736244	130,271 (24,861)	172,425 (32,980)	342,017 (65,676)
No multigrid, explicit	did not completely converge			
Multigrid, V-cycle, implicit	0.736007	4,718 (429)	5,939 (540)	26,539 (2,418)
No multigrid, implicit	0.737074	37,865 (5,895)	50,062 (7,793)	101,617 (15,895)

Table 4: Summary of the convergence characteristics of various solution techniques for computing a viscous turbulent flow around the RAE 2822 rectangular wing at  $M_\infty = 0.75$ ,  $\alpha = 2.72^\circ$ ,  $Re_L = 6.2 \times 10^6$ .

Solution technique	Memory* (words/cell)	Time/iteration (Alpha EV6-667 CPU seconds)
Multigrid, V-cycle, explicit	112	5.2
No multigrid, explicit	71	2.6
Multigrid, V-cycle implicit	236	10.9
No multigrid, implicit	193	6.4

Table 5: Memory and CPU time per iteration required by various solution techniques for computing a viscous turbulent flow around the RAE 2822 rectangular wing at  $M_\infty = 0.75$ ,  $\alpha = 2.72^\circ$ ,  $Re_L = 6.2 \times 10^6$ .

\* The numbers in this column do not represent a typical viscous case. See the details of the grid in the case description.

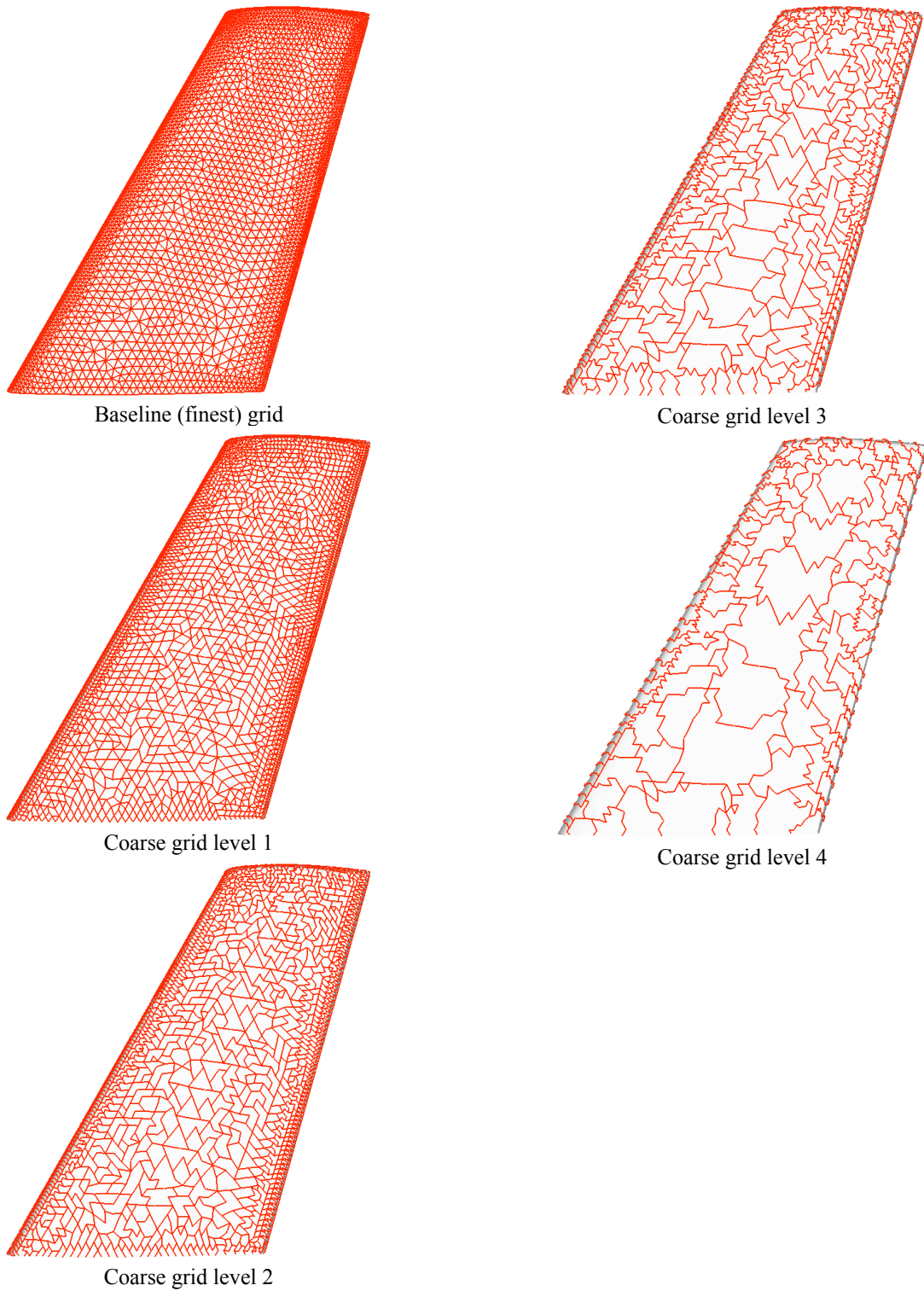
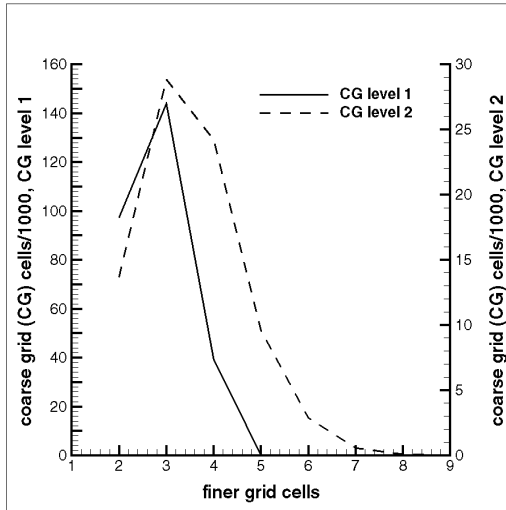
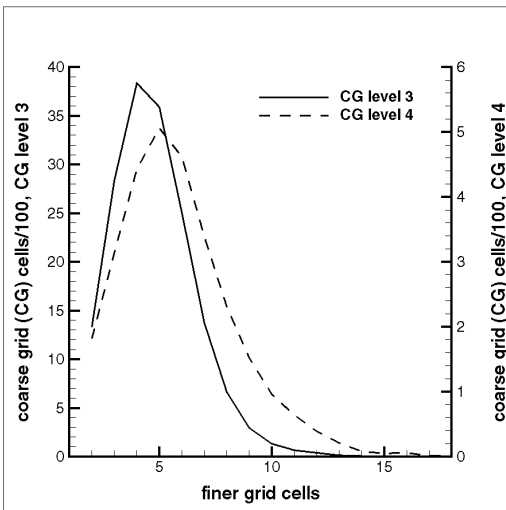


Figure 1: Surface grids on the ONERA M6 wing corresponding to the baseline grid and four coarser agglomerated grids.



coarse grid level 1 and 2



coarse grid level 3 and 4

Figure 2: Histogram displaying the distribution of fine grid cells in a coarser agglomerated grid for the ONERA M6 wing.

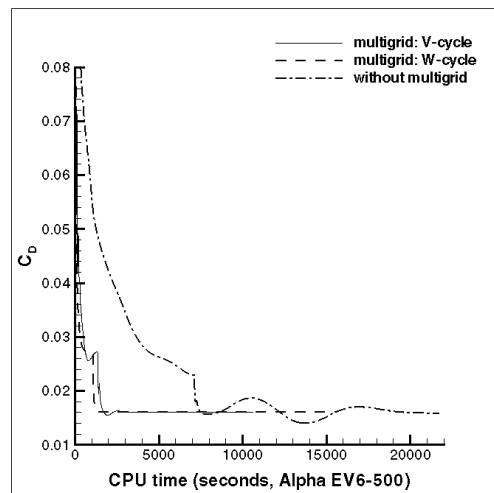
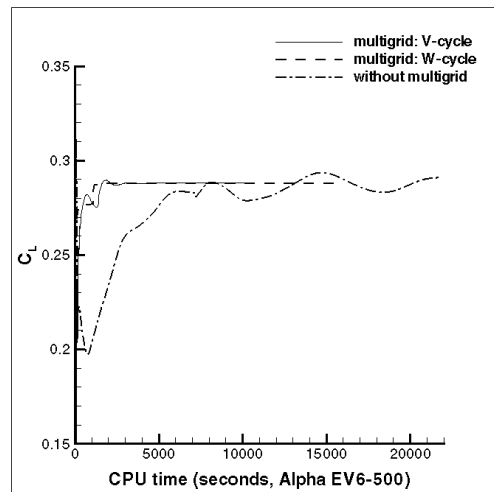
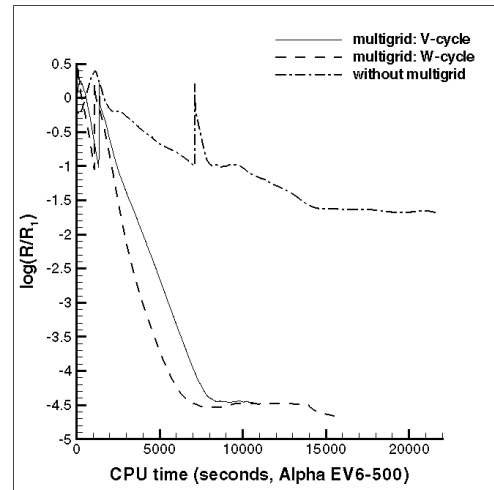


Figure 3: Convergence history of the V- and W-cycle multigrid explicit and the baseline explicit inviscid solutions obtained for the ONERA M6 wing at  $M_\infty = 0.84$ ,  $\alpha = 3.06^\circ$ .

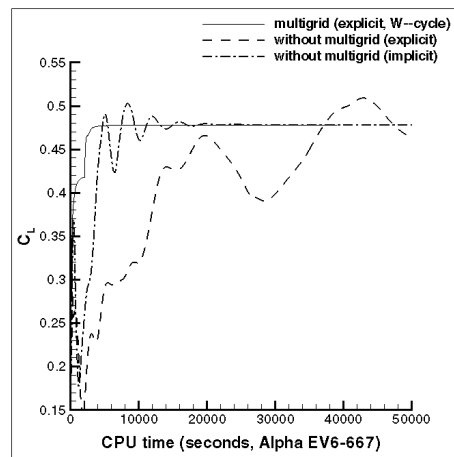
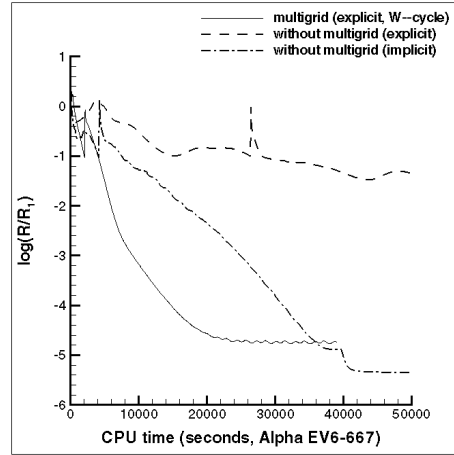
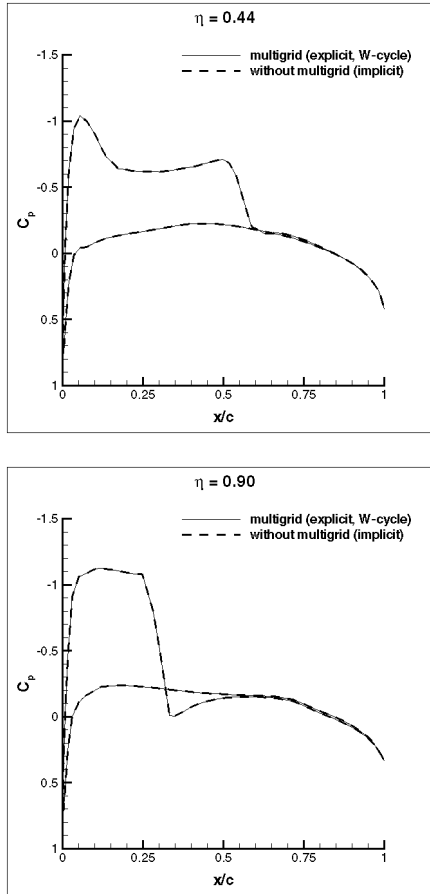


Figure 4: Comparison of the surface pressure coefficients corresponding to the W-cycle multigrid explicit and the baseline implicit inviscid solutions at two span wise cross-sections of the ONERA M6 wing at  $M_\infty = 0.84$ ,  $\alpha = 3.06^\circ$ .

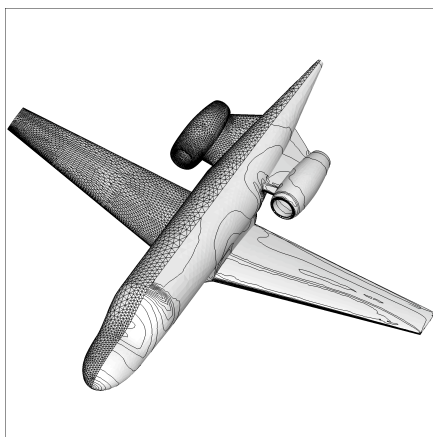


Figure 5: Surface grid corresponding to the baseline grid and surface Mach number corresponding to the W-cycle multigrid explicit inviscid solution for a generic business jet configuration at  $M_\infty = 0.75$ ,  $\alpha = 3.0^\circ$ .

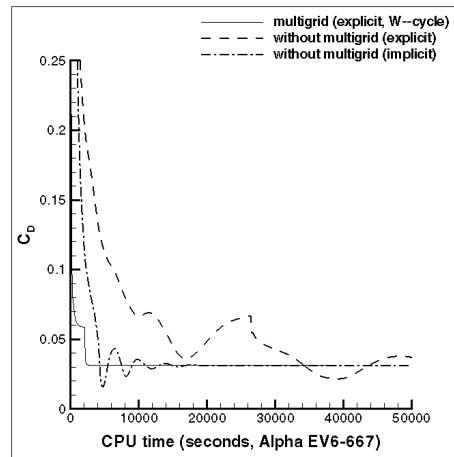


Figure 6: Convergence history of the W-cycle multigrid explicit, the baseline explicit and the baseline implicit inviscid solutions obtained for a generic business jet configuration at  $M_\infty = 0.75$ ,  $\alpha = 3.0^\circ$ .

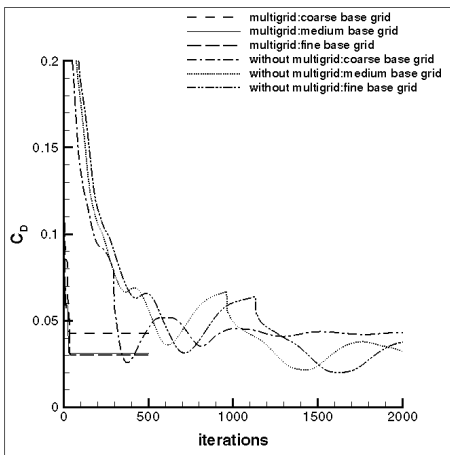
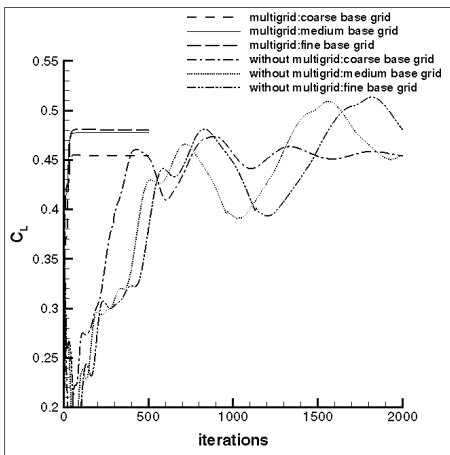
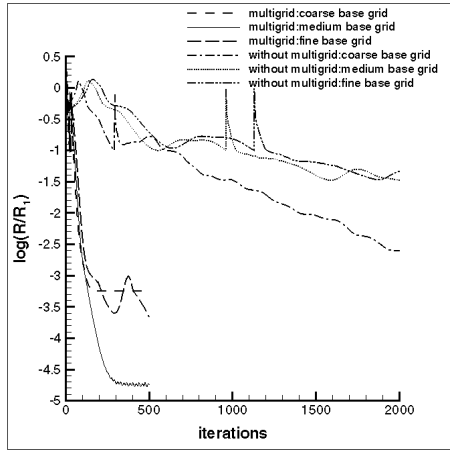


Figure 7: Convergence history of the W-cycle multigrid explicit and the baseline explicit inviscid solutions obtained using three baseline grids of varying density for a generic business jet at  $M_\infty = 0.75$ ,  $\alpha = 3.0^\circ$ .

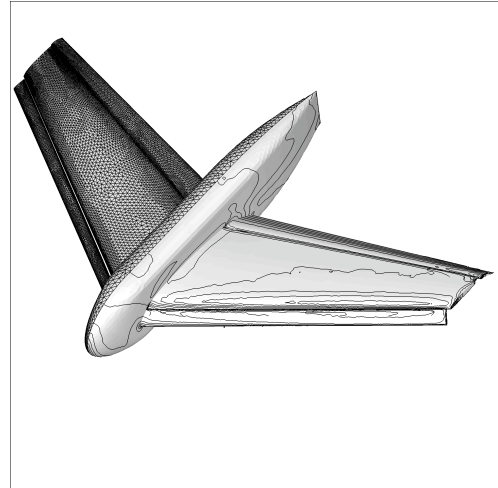


Figure 8: Surface grid corresponding to the baseline grid and surface Mach number corresponding to the W-cycle multigrid explicit inviscid solution for a generic high-lift trapezoidal wing at  $M_\infty = 0.20$ ,  $\alpha = 8^\circ$ .

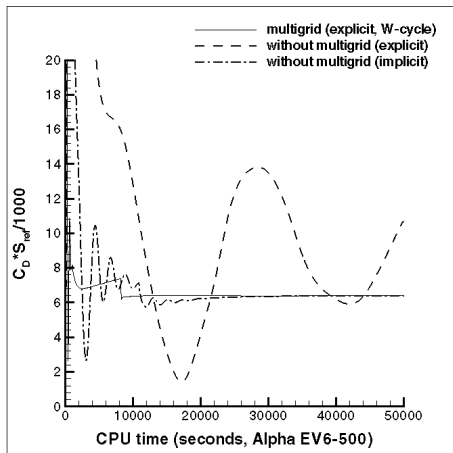
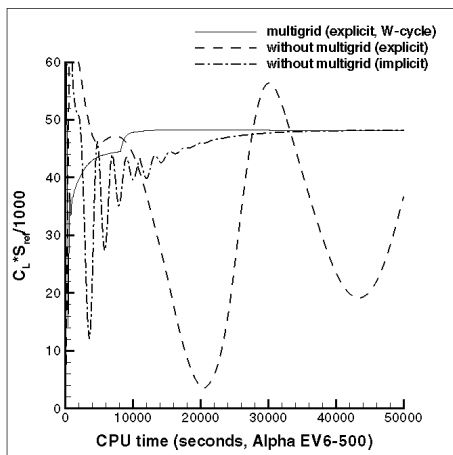
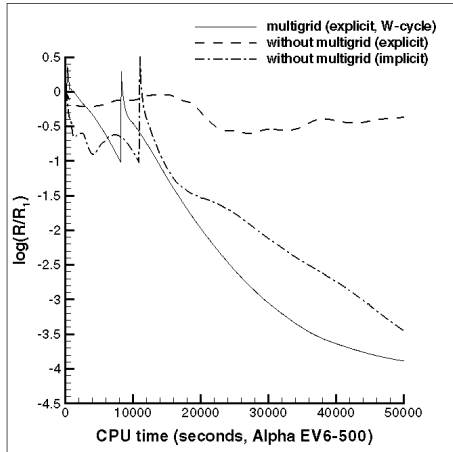
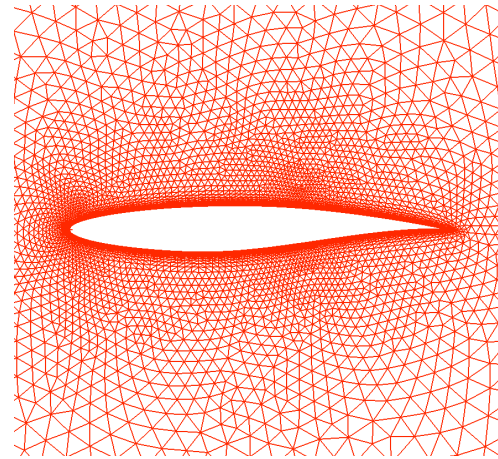
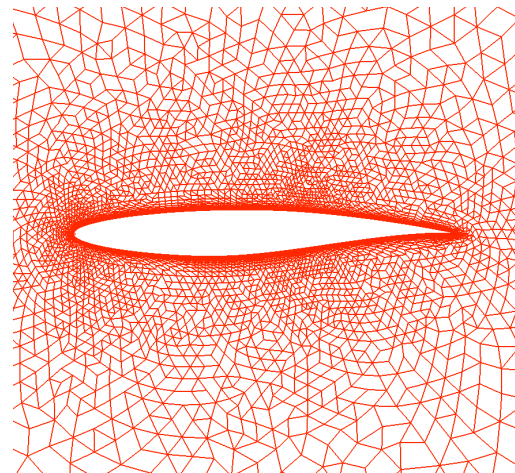


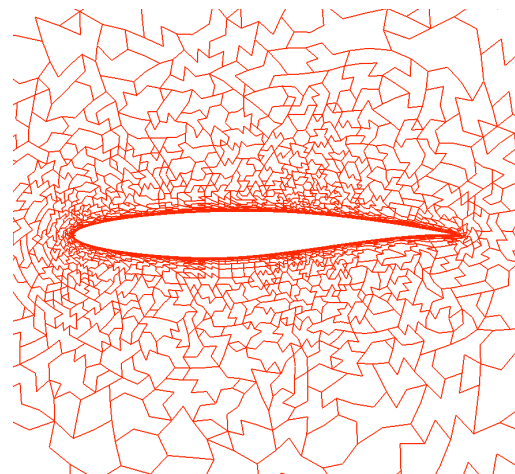
Figure 9: Convergence history of the W-cycle multigrid explicit, the baseline explicit and the baseline implicit inviscid solutions obtained for a generic high-lift trapezoidal wing at  $M_\infty = 0.20$ ,  $\alpha = 8^\circ$ .



Baseline (finest) grid



Coarse grid level 1



Coarse grid level 3

Figure 10: Close-up view of the baseline grid and the first and the third level coarse grids on a span wise end wall for the RAE 2822 rectangular wing.

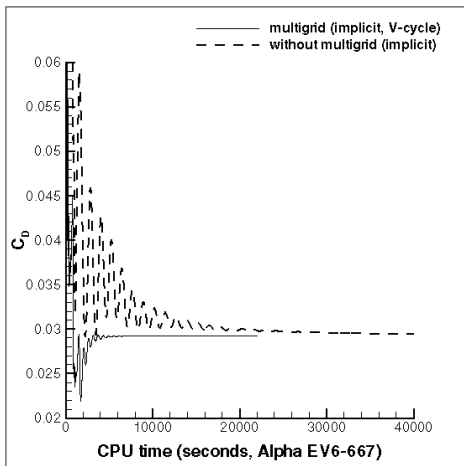
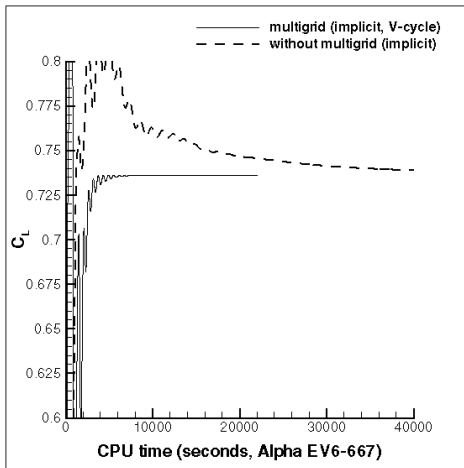
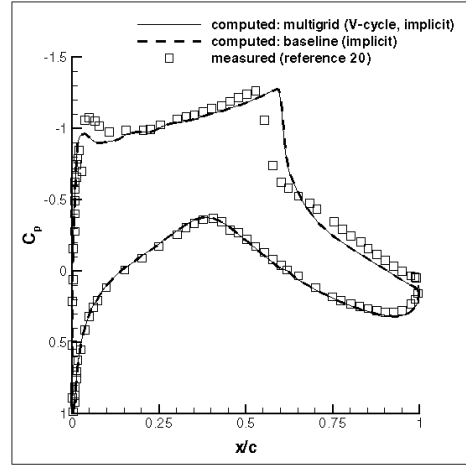
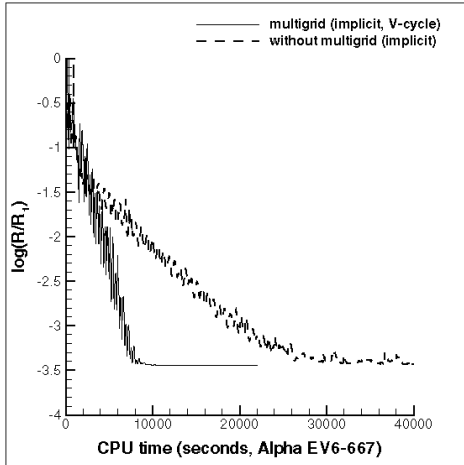


Figure 12: Comparison of the surface pressure coefficients corresponding to the V-cycle multigrid implicit and the baseline implicit viscous turbulent flow solutions and the measurements obtained for the RAE 2822 rectangular wing at  $M_\infty = 0.75$ ,  $\alpha = 2.72^\circ$ ,  $Re_L = 6.2 \times 10^6$ .

Figure 11: Convergence history of the V-cycle multigrid implicit and the baseline implicit viscous turbulent flow solutions obtained for the RAE 2822 rectangular wing at  $M_\infty = 0.75$ ,  $\alpha = 2.72^\circ$ ,  $Re_L = 6.2 \times 10^6$ .